

Natarajan, Elango, Meena, Liew, Markandan, Kalaimani, Anbuchezhiyan, Gnanasambandam, Ramesh, S. and Mohan, Dhanesh G (2026) Fracture mechanisms of PLA-HAp-MgO composites: Experimental characterisation and phase-field simulation. Journal of Materials Research and Technology, 44. pp. 3695-3706. ISSN 2238-7854

Version: VOR

Available under license: Creative Commons: Attribution 4.0

Downloaded from: https://sure.sunderland.ac.uk/id/eprint/20889/

Which version am I reading (articles, book chapters and books)

Pre-print (or submitted version): the version of an article or chapter before any peer-review. Can be submitted to a publisher or added to a pre-print server.

AAM: Author Accepted Manuscript - The version of the article formally accepted for publication after the peer-review process. It includes the changes made by the author(s) in line with peer-reviewers' comments. It has not undergone the publisher's formatting, type-setting and copyediting.

VOR: Version of Record - The version published on the publisher's website which includes formatting, typesetting and copyediting.

Usage guidelines

Please refer to the usage guidelines at http://sure.sunderland.ac.uk/policies.html or alternatively

contact sure@sunderland.ac.uk.

Journal of Materials Research and Technology 44 (2026) 3695–3706

Contents lists available at ScienceDirect

Journal of Materials Research and Technology

journal homepage: www.elsevier.com/locate/jmrt

Fracture mechanisms of PLA-HAp-MgO composites: Experimental characterisation and phase-field simulation

Elango Natarajan [a,*], Liew Meena [a], Kalaimani Markandan [a], Gnanasambandam Anbuchezhiyan [b], S. Ramesh [c], Dhanesh G. Mohan [d]

[a] Faculty of Engineering, Technology and Built Environment, UCSI University, Kuala Lumpur, Malaysia
[b] Department of Mechanical Engineering, Vel Tech Rangarajan Dr. Sagunthala R & D Institute of Science and Technology, Tamilnadu, Chennai, India
[c] Department of Mechanical Engineering, School of Engineering, Presidency University, Bengaluru, India
[d] School of Engineering, Faculty of Technology, University of Sunderland, Sunderland, United Kingdom

ARTICLE INFO

Keywords:
PLA
HAp
MgO
Sustainable material
Sustainable manufacturing
Product innovation

ABSTRACT

This study investigates the effect of hydroxyapatite (HAp) and magnesium oxide (MgO) dual fillers on the mechanical, thermal, and fracture behaviour of polylactic acid (PLA) composites through experimental characterisation and numerical simulations. PLA-HAp-MgO composites were fabricated via injection moulding with a fixed HAp content of 15 wt% and MgO contents ranging from 1 to 7 wt%. Results showed that 3 wt% MgO provided the optimum performance, increasing yield strength and ultimate tensile strength by 82.09% and 54.65%, respectively, compared with PLA-HAp. Thermal analysis using TGA/DTG/DSC showed that MgO incorporation modified the degradation behaviour of the PLA-HAp matrix. Particularly, the 3 wt% MgO composite exhibited a high-temperature DTG peak at 487.5 °C, indicating improved resistance to rapid mass loss and enhanced thermal response. Finite element simulations reproduced the experimental tensile response with deviations below 5%, validating the predictive capability of the numerical model. Phase-field fracture simulations revealed a composition-dependent trade-off between stiffness and fracture behaviour. The 3 wt% MgO composite delayed crack initiation but exhibited brittle-dominant fracture through damage localisation, whereas higher MgO loadings (5-7 wt%) promoted more gradual crack propagation. To this end, the dual HAp-MgO reinforcement significantly improved the strength, stiffness, and thermal resistance of PLA composites while providing insight into fracture mechanisms through the experimentally validated numerical simulation.

1. Introduction

As a thermoplastic, polylactic acid (PLA) that is derived from the α-hydroxy acid family via fermentation of plant starches (e.g., corn, sugarcane, or potatoes), acts as a greener alternative to traditional petrochemical-based polymers. It has gained significant research interest due to its environmentally friendly characteristics, including biodegradability and high composability [1]. Besides, With a density of approximately 1.24 g/cm^3, it exhibits good mechanical strength (~50 MPa) and a high elastic modulus (~2.0 GPa), enabling eco-friendly applications such as packaging and biomedical devices [2–4]. Furthermore, its excellent thermal stability supports most of the manufacturing techniques like melt extrusion, film casting, blow moulding, and fiber spinning. However, its low impact toughness, inherent brittleness, and limited use temperature hinder broader applications [5].

To overcome the limitations, polymer blending offers a convenient physical modification approach by incorporating different polymers or nanofillers into PLA to generate PLA composite with enhanced properties. For example, Hinchcliffe et al. reported that jute fiber increased the specific tensile strength and stiffness of neat PLA by 116% and 62%, respectively [6]. Aishah et al. found that a 90:10 PLA/recycled HDPE blend enhanced tensile modulus by 12.2% [7]. while Lu et al. showed that 30 wt% glass fiber improved PLA-HDPE tensile strength by 75.32% and thermal degradation temperature by 17 °C [8]. Two other potential fillers as reinforcement in PLA matrix are hydroxyapatite (HAp) and magnesium oxide (MgO), which can enhance mechanical, thermal, and bioactive properties for advanced applications. HAp, with an elastic modulus up to 120 GPa and compressive strength of 200 MPa, mimics bone mineral content and promotes cell attachment in biomedical uses like tissue engineering and implants [9,10]. A study by Tsuchiya et al.

* Corresponding author.
E-mail address: elango@ucsiuniversity.edu.my (E. Natarajan).

https://doi.org/10.1016/j.jmrt.2026.08.050
Received 31 March 2026; Received in revised form 26 June 2026; Accepted 7 August 2026
Available online 8 August 2026
2238-7854/© 2026 The Authors. Published by Elsevier B.V. This is an open access article under the CC BY license (http://creativecommons.org/licenses/by/4.0/).

demonstrated that porous HAp-collagen implants enabled cortical bone repair in rabbit models, with larger pore interconnections facilitating tissue invasion and rapid bone formation [11]. Murugan et al. used HAp to successfully synthesize orthopaedic implant hybrid material with polycaprolactone (PCL) and graphene oxide (M-HAP/PCL/GO) [12].

MgO features a high elastic modulus (up to 100 GPa), thermal conductivity of 50 W/m·K, and melting point of 2800 °C, considers it as a strong reinforcing filler that boosts the composite's thermal stability and mechanical strength. In addition to its reinforcing capability, recent studies have reported that MgO can influence the structural evolution of PLA-based materials through effects on crystallization behaviour, chain mobility, interfacial interactions, and processing-induced reactions. These mechanisms have been shown to affect the thermal, mechanical, and functional performance of PLA blends and nanocomposites. Therefore, MgO may contribute to composite behaviour through both physical reinforcement and microstructural modification of the PLA matrix [13–15]. In a study by Zhao et al., 1 wt% MgO increased the elastic modulus and tensile strength of PLLA by 78% and 17%, respectively with 77% increased crystallinity [16]. Likewise, Cament et al. demonstrated that 10 wt% MgO enhanced LDPE's elastic modulus by 48% and provided antimicrobial activity against *Escherichia coli* up to 53% efficiency [17]. Although PLA composites reinforced with HAp and MgO-based fillers have been reported, limited studies have combined systematic experimental characterisation with finite element and phase-field fracture simulation to evaluate the mechanical, thermal, morphological, and fracture behaviour of PLA-HAp-MgO composites.

In this context, the present work makes three main contributions. First, we provide systematic experimental characterisation of PLA composites with dual HAp–MgO fillers (varying 1-7 wt% MgO, fixed 15 wt% HAp), quantifying effects on morphology, mechanical performance and thermal stability and identifying an optimum wt.% MgO with substantially enhanced strength, stiffness, and degradation temperature relative to PLA-HAp. Second, we develop and validate an elastic finite element model reproducing experimental tensile responses with agreed <5% deviations, demonstrating that experimentally determined elastic properties are sufficient to accurately predict macroscopic stress-strain behaviour. Third, we implement a phase-field fracture framework to elucidate crack initiation and propagation mechanisms as a function of MgO content, revealing a clear trade-off between stiffness/strength and fracture stability and providing mechanistic guidelines for tailoring the fracture behaviour of PLA-based composites. Collectively, these contributions establish a combined experimental–numerical methodology for the design of sustainable PLA-HAp-MgO composites for structural and biomedical applications.

2. Experimental design

2.1. Materials and Method

Medical grade PLA pellets (3 mm average size), MgO particles (250 nm), and HAp particles (80 nm) were sourced from Sigma-Aldrich. The average melting point of PLA, HAp and MgO particles are 170 °C, 1100 °C and 2800 °C respectively. All the chemicals were used as purchased and without further purification. All PLA matrix composites maintained a fixed HAp concentration of 15 wt%, while MgO levels varied at 1, 3, 5, and 7 wt% as detailed in Table 1. The HAp content was fixed at 15 wt% based on previous studies reporting favourable mechanical performance and processability of the composites at this concentration [18]. MgO loadings of 1-7 wt% were selected to investigate the effect of MgO addition on composite properties and to identify the optimum loading before excessive particle agglomeration occurs. Prior to blending and injection moulding, PLA pellets were dried at 60 °C for 4 h, while HAp and MgO powders were dried at 80 °C for 12 h to minimise moisture uptake and prevent hydrolytic degradation during processing. The dried PLA, HAp, and MgO constituents were premixed using a tumble mixer, followed by fabrication using a vertical plastic injection moulding machine, MATHMAN MPR750R2, China as reported in our previous studies [19,20].

Table 1
Composite designation and wt% of MgO.

Designation	PLA (wt. %)	HAp (wt. %)	MgO (wt. %)
PLA-HAp	85	15	0
PLA-HAp-MgO1	84	15	1
PLA-HAp-MgO3	82	15	3
PLA-HAp-MgO5	80	15	5
PLA-HAp-MgO7	78	15	7

The moulding chamber temperature was set to 160 °C for crystallization of polymers. The injection temperature and pressure in the moulding machine were set at 220 °C and 50 bar, respectively, to introduce the semi-pressurized PLA matrix blended with fillers (HAp and MgO) into the die cavity. Similar to our previous study, the injection time (10 s), cooling time (40 s) and ejection time (2 s) were maintained and the samples were removed from die cavity once injection moulding was done. The samples for mechanical tests were then cut as per ASTM standards. Schematic illustration of the injection moulding setup is shown in Fig. 1.

2.2. Characterizations

Thermogravimetric analysis and differential scanning calorimetry (TGA/DSC) were performed using a NETZSCH STA 449 F3 simultaneous thermal analyser. Samples were heated from approximately 28 °C to 1000 °C at a heating rate of 20 K/min using DSC/TG sample carriers and alumina crucibles. The measurements were conducted under nitrogen atmosphere throughout the test. The TGA curves were used to evaluate mass-loss behaviour and residual mass, while the corresponding DTG curves were derived from the TGA data to identify the temperature associated with the maximum degradation rate. DSC curves were used as supporting thermal evidence to identify heat-flow events associated with polymer degradation and filler-related thermal transitions. To ensure measurement reliability, the instrument was calibrated according to the manufacturer's procedures before testing, and all samples were tested under identical experimental conditions.

A JASCO FT/IR-6300 (Japan) Type A Fourier transform infrared (FTIR) spectrometer was used in attenuated total reflectance (ATR) mode to identify chemical interactions and functional groups, scanning from 4000 to 500 cm^{-1} at 4 cm^{-1} resolution (32 scans per sample). Surface morphology and fracture surfaces (post-tensile/flexural testing) were examined using a JEOL JSM-7600F (Japan) at 2-5 kV after sputter coating with ~5 nm Au-Pd. Samples were observed at 500x to 1000x magnification.

X-ray diffraction (XRD) analysis was conducted to identify the crystalline phases present in the PLA-HAp and PLA-HAp-MgO composites. The XRD measurements were performed using a PANalytical XPERT-3 diffractometer equipped with a reflection transmission spinner stage. The samples were scanned in continuous mode over a 2θ range of 5.0066° to 89.9876° using Cu Kα radiation. The operating voltage and current were maintained at 45 kV and 30 mA respectively. The step size was 0.0130° 2θ, and the scan step time was 48.195 s. Measurements were carried out at room temperature using a spinning sample stage to improve counting statistics and reduce preferred-orientation effects. The obtained diffraction patterns were analysed qualitatively to confirm the presence of crystalline inorganic phases, particularly HAp and MgO reflections and to examine whether new crystalline phases were formed after MgO incorporation.

Elastic modulus (E), 0.2% offset yield strength and ultimate tensile strength (σ) of the composite were measured as per ASTM D638 using an Instron 5985 (n = 3 per composition). Flexural strength, bending modulus, and strain were determined as per ASTM D790 using 3-point bending (100 mm × 20 mm × 5 mm) at 2 mm/min (n = 3 per

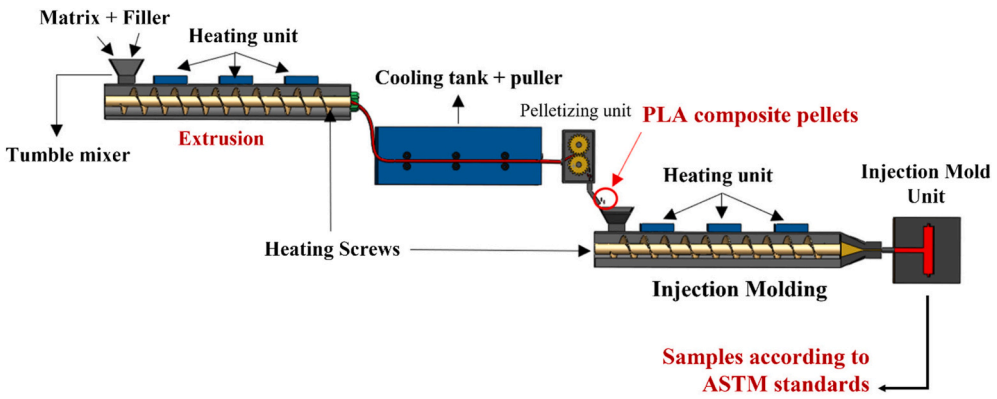


Fig. 1. Injection moulding process illustrated.

composition). The density of each composite was determined experimentally from the measured mass and specimen dimensions. The volume was calculated from the specimen geometry, and density was obtained as the ratio of mass to volume and subsequently used for the Ashby chart analysis.

2.3. Numerical simulations

2.3.1. Finite element analysis (FEA)

Linear finite element analysis was performed using COMSOL Multiphysics 6.2 (Solid mechanics module) to replicate the experimental tensile tests. The dumbbell tensile specimen was meshed with 2D triangular element using the physics-controlled mesh setting under General Physics. A 2D plane-stress formulation was adopted because the tensile specimens were thin relative to their gauge length and width, and the dominant deformation during uniaxial tensile loading was assumed to occur in the in-plane direction. The model therefore captures the macroscopic stress distribution and relative crack-initiation behaviour.

The mesh size was selected as extremely fine to ensure better accuracy in capturing the stress distribution, especially at the gauge section where failure is expected to occur. The whole model had about 41,017 elements with the maximum size = 1.05 mm, and the minimum size = 0.00211 mm and maximum element growth rate = 1.1. The maximum growth rate helped to allow a smooth transition between large and small elements. The curvature factor was defined as 0.2 so that the curved shoulder regions of the specimen could be captured properly. The resolution of narrow regions was set to 1 to improve the mesh quality at the reduced cross-section area. Mesh convergence was verified by ensuring <1% change in max. Stress with progressive refinement. One grip end was fixed $(u_x = 0, u_y = 0)$, while the opposite end received ramped axial displacement (quasi-static rate equivalent to 5 mm/min, total ~5% strain). Material properties such as elastic modulus (E), poison ratio (υ), and density (ρ) were assigned per composition. Maximum von Mises stress (σ) at failure was extracted for validation against the ultimate strength of the material (S_{ut}) within deviation <5%.

2.3.2. Phase-field fracture modelling

Crack initiation/propagation was simulated using a phase-field approach (isotropic damage model) coupled to the elastic FEA framework. The fracture energy (G_c) was calibrated from experimental (S_{ut}) and (E), per composition $G_c \approx \frac{S_{ut}{}^2}{E}$, length scale $l = 0.5$ mm). The phase-field order parameter d (0 = undamaged, 1 = fully broken) evolved via the AT2 (Ambrosio-Tortorelli 2) model. Damage initiated when tensile strain energy exceeded G_c, driving diffuse crack evolution without predefined paths. Simulations used the same geometry/mesh as FEA with history-field tracking to enforce irreversibility. It should be noted that this approximation provides only an estimated fracture energy based on macroscopic tensile properties and does not fully account for microstructural effects such as particle dispersion, filler–matrix debonding, agglomeration, and crack deflection. Therefore, the calculated G_c values were used as comparative calibration parameters for the phase-field model rather than as experimentally measured fracture toughness values. Moreover, the phase-field results are used for qualitative mechanistic interpretation rather than quantitative fracture validation.

3. Results and discussion

3.1. Morphological characterization

Fig. 2 shows the SEM results of neat PLA-HAp and PLA-HAp-MgO composites. Neat PLA-HAp (Fig. 2A) exhibited a smooth surface morphology, reflecting uniform embedding of HAp particles within the PLA matrix without excessive roughness. In contrast, MgO reinforcement introduced surface texturing and increased roughness (Fig. 2B–E), with protruding MgO particles creating irregular topography. Low MgO contents (1-5 wt%, Fig. 2B–D) showed relatively continuous surface morphology with less obvious filler clustering than the 7 wt% MgO composite, suggesting improved filler dispersion and physical filler–matrix contact. This morphology may support more effective load sharing between the PLA matrix and the inorganic fillers. At 7 wt% MgO (Fig. 2E), clumping of particles (agglomeration) was evident, forming filler clusters that disrupt matrix continuity and act as stress concentrators. This caused decline in mechanical properties as evidenced and discussed in Section 3.5.

3.2. FTIR analysis

Fig. 3 shows the FTIR spectra of PLA-HAp and PLA-HAp-MgO composites. All composites exhibited characteristic peaks at 1088 cm^{-1} (P-O stretching of the phosphate group, PO_4^{3-}, from HAp), 1181 cm^{-1} (C-O stretching of the PLA ester group), 1456 cm^{-1} (C-H bending of CH_3 in PLA), and 1752 cm^{-1} (C═O stretching of the PLA ester carbonyl group) [21,22]. Variations in band intensity were observed, particularly near 2917 cm^{-1}, corresponding to C-H stretching vibrations, which may be associated with compositional changes caused by MgO incorporation into the PLA-HAp matrix. However, no new absorption bands or significant peak shifts were detected, indicating that the addition of MgO did not substantially alter the chemical structure of PLA. Therefore, the observed improvements in mechanical and thermal properties are primarily attributed to physical filler reinforcement and microstructural effects rather than the formation of new chemical interactions among the constituents.

3.3. XRD

Fig. 4 shows the XRD patterns of PLA-HAp and PLA-HAp-MgO

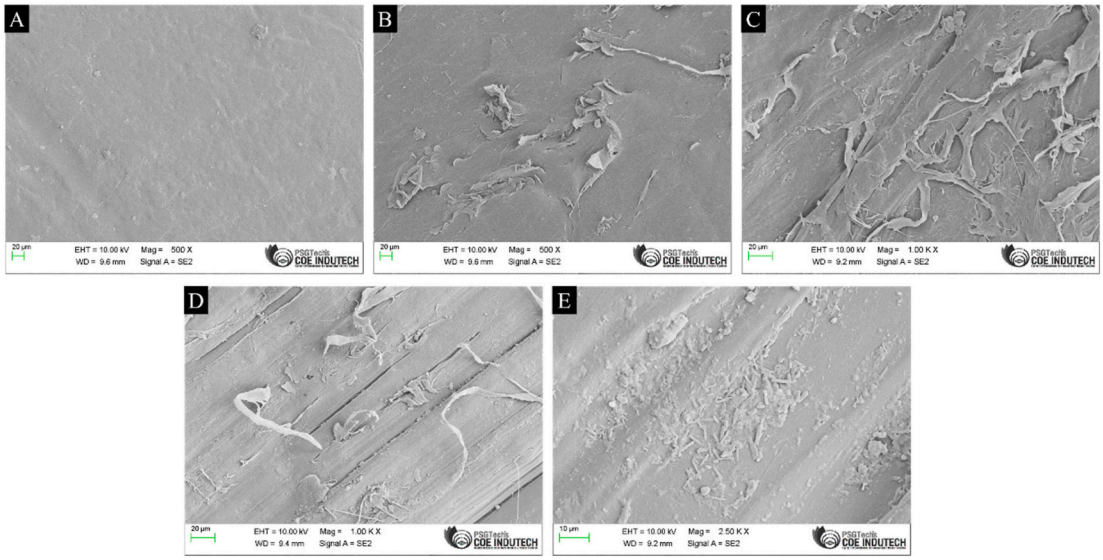


Fig. 2. Morphology plots of (A) neat PLA-HAp (B) PLA-HAp-MgO1 (C) PLA-HAp-MgO3 (D) PLA-HAp-MgO5 and (E) PLA-HAp-MgO7.

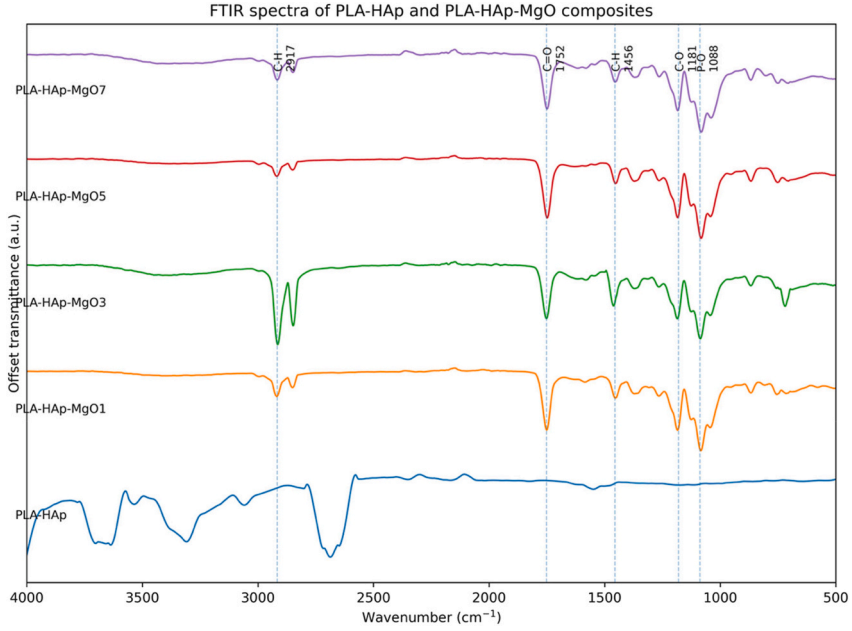


Fig. 3. FTIR spectra of neat PLA-HAp and PLA-HAp-MgO composites.

composites with different MgO loadings. The XRD measurements were carried out using Cu Kα radiation over a 2θ range of approximately 5-90°. The PLA-HAp composite showed broad diffraction features in the lower 2θ region, particularly around 16-24°, indicating the presence of the polymer matrix together with the inorganic HAp phase. The broad nature of these features suggests that the composite retained a largely polymer-dominated structure with dispersed inorganic filler phases. With the incorporation of MgO, additional crystalline reflections were observed in the MgO-reinforced composites. The XRD phase identification confirmed the presence of magnesium oxide/periclase-related crystalline phases in the MgO-reinforced samples. This confirms that MgO remained as a crystalline filler phase after injection moulding and was not completely transformed or degraded during processing. The persistence of MgO-related reflections supports the role of MgO as a rigid inorganic reinforcement within the PLA-HAp matrix.

The presence of MgO/periclase-related peaks in MgO-reinforced composites further supports the mechanical results. At low to moderate MgO loading, especially 3 wt% MgO, the retained crystalline MgO phase can act as a rigid load-bearing filler within the PLA-HAp matrix. This contributes to improved stiffness, load sharing, and resistance to deformation, which is consistent with the observed increase in tensile strength, yield strength, and flexural strength. However, at higher MgO loadings, the mechanical properties decreased despite the continued presence of crystalline MgO. This indicates that the reinforcing effect of MgO is not governed only by its crystalline phase, but also by its dispersion quality within the polymer matrix. The SEM results showed particle agglomeration at higher MgO content, which can create local stress-concentration sites and reduce the effective load-bearing capacity of the composite.

3.4. Thermal analysis: TGA, DTG, and DSC

Fig. 5A shows the thermogravimetric analysis (TGA) curves of PLA-HAp-MgO composites with different MgO loadings, while Fig. 5B

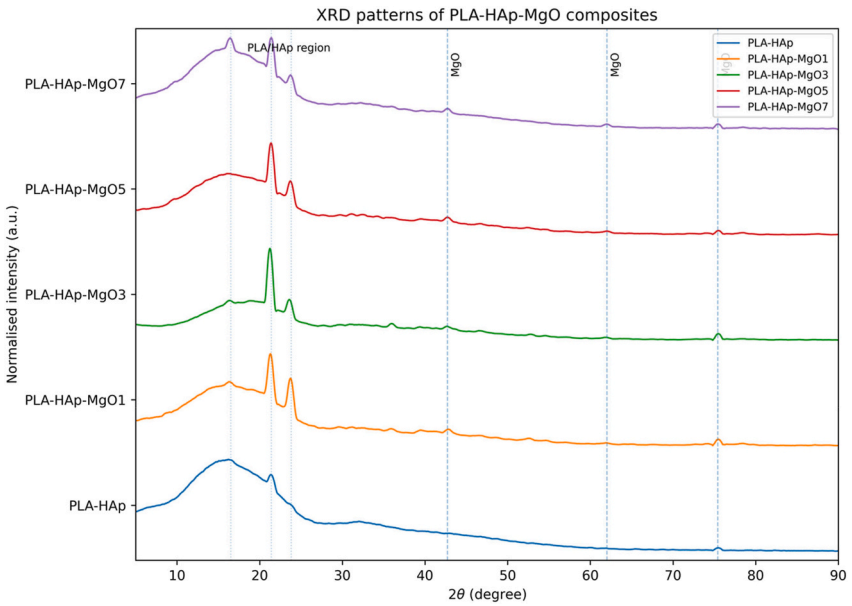


Fig. 4. XRD patterns of PLA-HAp and PLA-HAp-MgO composites with different MgO loadings, showing polymer-related broad diffraction features and MgO/periclase-related crystalline reflections in MgO-containing composites.

presents the corresponding derivative thermogravimetric (DTG) curves. The DSC curves are shown in Fig. 5C.

The TGA curves show that all PLA-HAp-MgO composites underwent a major mass-loss between approximately 280 °C and 330 °C, which is mainly associated with thermal degradation of the PLA matrix. The corresponding DTG curves were used to identify the maximum degradation-rate temperature T_{max}, because DTG provides a clearer indication of the temperature at which the highest mass-loss rate occurs. The PLA-HAp-MgO1 composite showed a main DTG peak at 313.0 °C and a secondary degradation event at 486.2 °C. The PLA-HAp-MgO5 and PLA-HAp-MgO7 composites showed main DTG peaks at 309.2 °C and 313.6 °C, respectively, with secondary high-temperature events at 466.1 °C and 485.5 °C. These results indicate that the primary degradation behaviour of the PLA-HAp-MgO system is governed mainly by degradation of the PLA matrix, while secondary high-temperature events are associated with further decomposition of intermediate degradation residues and the thermal response of the inorganic-filled composite structure.

The PLA-HAp-MgO3 composite exhibited a different degradation profile compared with the other compositions. Although a lower-temperature degradation event was observed at 310.8 °C, the strongest DTG peak appeared at 487.5 °C. This indicates that the 3 wt% MgO composite exhibited a pronounced high-temperature degradation, suggesting enhanced resistance to rapid mass loss at the primary degradation stage. This behaviour is consistent with the superior mechanical performance of the same composition, where 3 wt% MgO produced the highest tensile strength, yield strength, and flexural strength. Therefore, the thermal and mechanical results together suggest that 3 wt% MgO provides the most favourable balance between filler reinforcement, physical filler–matrix contact, and restriction of PLA chain mobility.

The thermal degradation parameters obtained from TGA/DTG and DSC analysis are summarised in Table 2.

The DSC curves further support the composition-dependent thermal behaviour of the composites. The PLA-HAp-MgO1 composite showed a major DSC peak at 314.3 °C, which agrees closely with its main DTG peak at 313.0 °C. The PLA-HAp-MgO3 composite exhibited multiple DSC events at 106.7, 283.3, and 456.6 °C, indicating a more complex thermal response. The high-temperature DSC event at 456.6 °C corresponds reasonably with the high-temperature DTG event observed for this composition. The PLA-HAp-MgO5 composite showed DSC peaks at 282.5 and 550.1 °C, while the PLA-HAp-MgO7 composite showed a major DSC peak at 319.2 °C. These DSC events confirm that MgO loading modifies the thermal response of the PLA-HAp matrix, most likely through changes in filler dispersion, restriction of polymer-chain mobility, and the barrier effect of thermally stable inorganic fillers.

The thermal behaviour is consistent with the FTIR and XRD results. FTIR analysis showed no new absorption bands or significant peak shifts after MgO incorporation, indicating that MgO addition did not produce major new chemical interactions within the PLA matrix. XRD analysis confirmed the retention of crystalline MgO/periclase-related phases in the MgO-containing composites. Therefore, the improved thermal response is attributed mainly to physical reinforcement, filler dispersion, physical filler–matrix contact, restricted PLA chain mobility, and the barrier effect of inorganic HAp and MgO phases rather than the formation of new chemical reaction products.

The PLA-HAp-MgO1, PLA-HAp-MgO3, and PLA-HAp-MgO7 composites showed residual masses of approximately 2.86%, 0.34%, and 0.51%, respectively, near 997 °C. However, the PLA-HAp-MgO5 TGA curve showed an unrealistic negative residual mass, indicating a baseline correction artefact. Therefore, the residual mass of PLA-HAp-MgO5 was not considered for quantitative interpretation. Overall, the TGA, DTG, and DSC results show that MgO addition modifies the thermal degradation behaviour of PLA-HAp composites, with the 3 wt% MgO composition showing the most favourable combined thermal and mechanical response.

3.5. *Mechanical properties of composites*

Fig. 6 shows the tensile and flexural stress-strain curves of PLA-HAp and PLA-HAp-MgO composites, while Tables 3 and 4 summarizes extracted tensile and flexural properties of composites.

The PLA-HAp-MgO3 (3 wt% MgO) composite showed the maximized tensile performance, boosting the ultimate tensile strength by 54.65% and yield strength of the composites at 0.2% offset by 82.09% relative to PLA-HAp composite (33.21 MPa). Elastic modulus peaked at 1 wt% MgO (+26.4%, from 3225.9 MPa to 4077.6 MPa), reflecting MgO's high intrinsic stiffness that enhances composite rigidity even at low loadings. The improved strength of the MgO-reinforced composites can be attributed to the physical reinforcing effect of dispersed MgO particles within the PLA-HAp matrix. At optimum loading, MgO particles may act

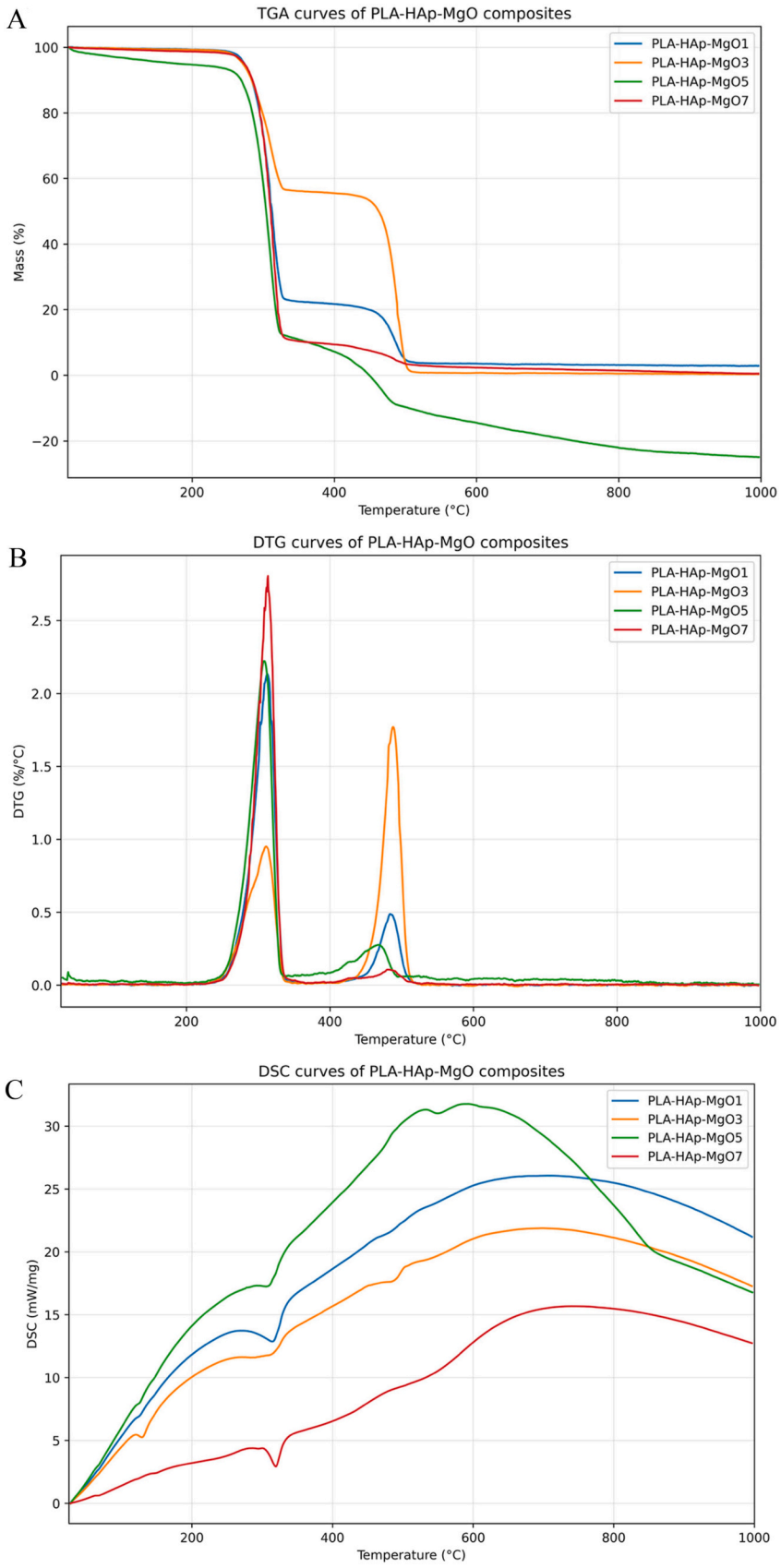


Fig. 5. Thermal analysis of PLA-HAp-MgO composites with different MgO loadings: (A) TGA curves showing mass-loss behaviour, (B) DTG curves showing maximum degradation-rate temperatures, and (C) DSC curves showing composition-dependent thermal events.

Table 2
Summary from TGA analysis.

Composite	Onset Temperature $T_{5\%}$ °C	Primary DTG event T_{max} °C	High-temperature DTG event °C	DSC Peak(s) °C	Residual mass at ~997 °C (%)
PLA-HAp-MgO1	273.6	313.0	486.2	314.3	2.86
PLA-HAp-MgO3	271.2	487.5	310.8	106.7, 283.3, 456.6	0.34
PLA-HAp-MgO5	178.7	309.2	466.1	282.5, 550.1	Not reported*
PLA-HAp-MgO7	273.4	313.6	485.5	319.2	0.51

Note: T_{onset} represents the temperature corresponding to 5% mass loss and is used as the onset degradation indicator. DTG peaks were calculated from the first derivative of the TGA mass-loss curves. The reported T_{max} values correspond to temperatures at maximum mass-loss rate. Residual mass for PLA-HAp-MgO5 was not reported because the corresponding TGA curve showed a negative residual mass, indicating baseline correction artefact.

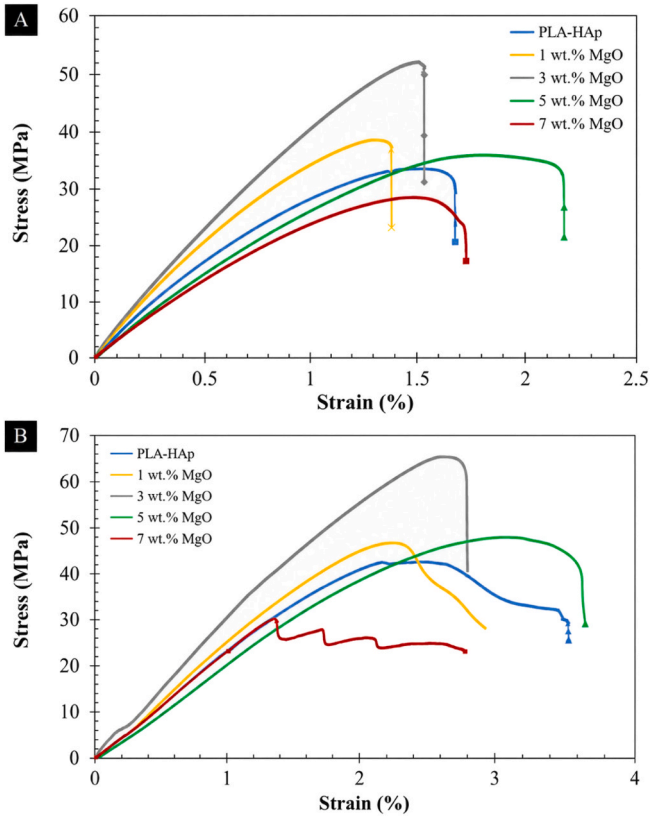


Fig. 6. Stress-strain curves (A) Tensile (B) Flexural.

as rigid load-bearing sites, restrict local deformation of PLA chains, and improve load sharing between the matrix and inorganic fillers through physical filler-matrix contact [20,23,24]. Both UTS and modulus declined at >3 wt% MgO due to particle agglomeration (Fig. 2E–Section 3.1), creating stress concentrators that promote early failure. The combined SEM and FTIR observations suggest that the reinforcement is mainly governed by filler dispersion, physical filler–matrix contact, and microstructural constraint rather than confirmed chemical bonding.

Flexural properties followed similar trends, with 3 wt% MgO increasing flexural strength by 54.5% (from 42.2 MPa to 65.2 MPa) and modulus by 29.1% (from 2454 MPa to 3169 MPa), confirming transverse load-bearing improvements from dual-filler reinforcement.

The improved flexural properties can be due to high stiffness and bone like structure of HAp as well as the high elastic modulus of MgO which enhanced rigidity and strength of the overall composite such that it is more resistant to bending and deformation under load [25,26]. Recent MgO-loaded PLA-based literature have also demonstrated that MgO can influence functional performance, structural evolution, and reactive blending behaviour in PLA-based systems [27,28].

3.5.1. SEM graphs of fractured samples

Fig. 7 shows the fractured surface morphologies. Neat PLA–HAp (Fig. 7A) displayed a smooth fracture surface with loosely bound HAp particles, characteristic of weak matrix–filler adhesion and brittle failure.

In contrast, the fractured PLA-HAp-MgO composites exhibited ductile fracture across 1 to 5 wt% loadings (Fig. 6B–D), evidenced by plastic deformation zones and less distinct cleavage planes. This indicates that addition of MgO particles helped to distribute load more effectively to prevent crack formation and led to higher energy dissipation at fracture surfaces to create a tough composite. The fracture-surface features suggest improved energy dissipation and load sharing in the low-to-moderate MgO composites, particularly at 3 wt% MgO (Table 3). This is most likely due to better filler dispersion and physical interaction between the PLA matrix and inorganic fillers. On the other hand, at higher MgO concentration (i.e.,7 wt%), the agglomeration of MgO particles would have disrupted matrix structure, It led to brittle dominated fracture mechanism, as demonstrated by the large cracks and fracture lines in the SEM images.

3.6. Numerical simulation of tensile behaviour

Maximum von Mises stress (σ) at failure was extracted for validation against the ultimate strength of the material (S_{ut}) within deviation <5%.

Table 4
Flexural properties of PLA-HAp and PLA-HAp-MgO composites.

	Flexural stress (MPa)	Flexural Modulus (MPa)	Flexural strain (%)
PLA-HAp	42.20 ± 2.01	2454.45 ± 48.13	1.95 ± 0.08
PLA-HAp-MgO1	46.35 ± 1.92	2619.45 ± 57.65	2.00 ± 0.09
PLA-HAp-MgO3	65.19 ± 2.32	3168.87 ± 59.74	2.07 ± 0.11
PLA-HAp-MgO5	47.57 ± 1.74	2331.69 ± 49.59	2.05 ± 0.10
PLA-HAp-MgO7	30.94 ± 1.87	2489.86 ± 50.37	1.44 ± 0.08

Table 3
Tensile properties of PLA-HAp and PLA-HAp-MgO composites.

	Ultimate tensile strength (MPa)	Young's Modulus (MPa)	Yield strength at 0.2% offset (MPa)	Tensile strain (%)
PLA-HAp	33.21 ± 1.78	3225.91 ± 50.41	27.80 ± 1.87	1.51 ± 0.08
PLA-HAp-MgO1	38.07 ± 2.01	4077.55 ± 62.18	32.78 ± 1.94	1.32 ± 0.07
PLA-HAp-MgO3	51.36 ± 2.84	4046.93 ± 58.72	50.62 ± 2.18	1.54 ± 0.11
PLA-HAp-MgO5	35.48 ± 1.64	2935.46 ± 47.95	28.99 ± 2.05	1.82 ± 0.13
PLA-HAp-MgO7	28.00 ± 1.67	2709.60 ± 54.91	24.14 ± 2.01	1.51 ± 0.09

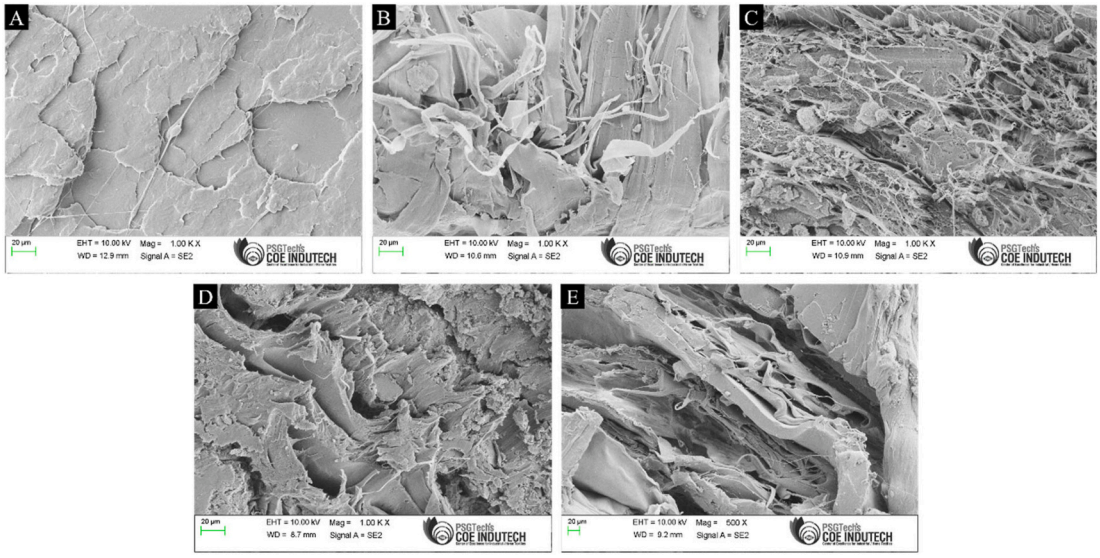


Fig. 7. Fractured surfaces of (A) neat PLA-HAp (B) PLA-HAp-MgO1 (C) PLA-HAp-MgO3 (D) PLA-HAp-MgO5 and (E) PLA-HAp-MgO7.

For PLA-HAp composite, the experimental tensile strength was 36.7 MPa while simulation closely reproduced the maximum stress as 38.1 MPa (3.8% deviation). For composites with 1 wt% MgO, experimental and simulated stresses were 41.5 MPa and 40.0 MPa, respectively (4.1% deviation).

From Fig. 8, the maximum von Mises equivalent stress (σ) in the gauge section of 3 wt% MgO was 53.4 MPa in the fillet–gauge transition (hotspot in the stress contour), closely matching experimental strength (55.7 MPa, 4.1% deviation). This close agreement across all compositions (see Table 5) confirms that experimentally derived elastic properties reliably predict macroscopic stress-strain behaviour under uniaxial loading. It should be noted that the experimental tensile strengths used for FEA validation in Table 5 correspond to representative specimens selected for numerical modelling, whereas Table 3 reports the mean ± standard deviation obtained from three specimens.

Table 5
Comparison between experimental and numerically simulated maximum tensile stresses of PLA-HAp-MgO composites under uniaxial loading.

Composite	Tensile Strength (MPa)		Variance (%)
	Experimental	COMSOL Simulation	
PLA-HAp	36.7	38.1	3.81%
PLA-HAp-MgO1	41.5	40	3.61%
PLA-HAp-MgO3	55.7	53.4	4.13%
PLA-HAp-MgO5	38.8	38.1	1.80%
PLA-HAp-MgO7	31.1	30.5	1.93%

3.7. Phase-field simulation of crack initiation and propagation

Phase-field fracture simulations extended the validated FEA framework (Section 3.4) to predict crack initiation and propagation in PLA-HAp-MgO composites without predefined crack paths. The phase-field order parameter d (0 = undamaged, 1 = fully broken) evolved according to local tensile strain energy via the AT2 model, using composition-specific G_c (fracture energy) calibrated from experimental $\frac{S_{ut}^2}{E}$ ratios and length scale $l = 0.5$ mm. The phase-field length-scale parameter ($l = 0.5$) mm was selected as a numerical regularisation parameter to obtain a stable diffuse crack representation while maintaining damage localisation within the gauge section of the tensile specimen. This value is consistent with length-scale values reported in previous phase-field

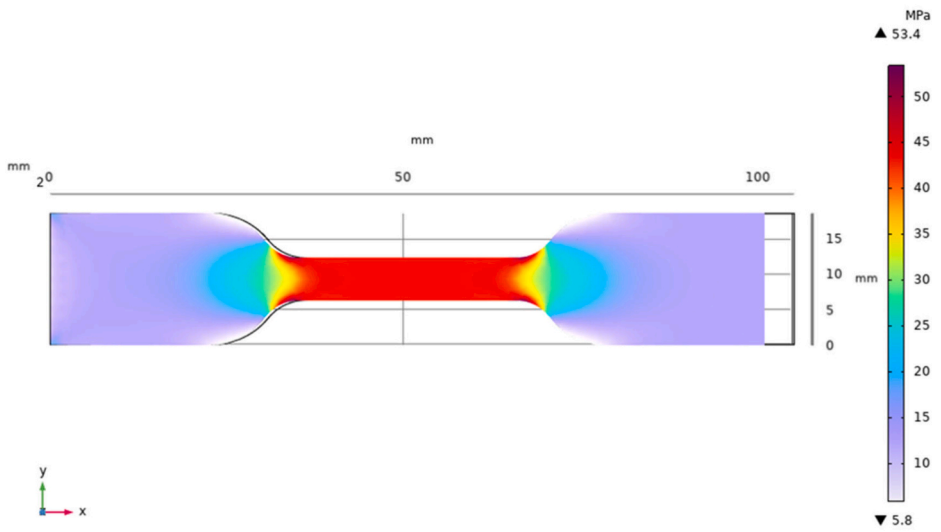


Fig. 8. Von Mises stress distribution of PLA-HAp-MgO3 composite under uniaxial tensile loading.

fracture studies. Hirshikesh et al. [29] used a comparable length-scale value of (l = 0.524) mm for phase-field modelling of crack propagation. In the phase-field formulation, (l) controls the width of the diffused damage zone. Smaller values produce sharper and more localised cracks but require finer meshes, whereas larger values result in wider damage bands and smoother crack propagation. Egger et al. [30] conducted a systematic length-scale and mesh-sensitivity analyses with 0.25, 0.5, 2, and 4 mm to assess their influence on fracture response. In the present study, the phase-field results are interpreted qualitatively to compare relative crack-initiation and propagation behaviour among compositions rather than as fully quantitative fracture predictions.

Fig. 9 shows the phase-field damage contours for PLA-HAp-MgO3 composite (3 wt% MgO) under uniaxial tensile loading. In elastic stage, the damage field is essentially zero (dark blue) everywhere, meaning the specimen is deforming elastically with no microcrack formation. Strain energy is building but remains below the critical threshold. During crack initiation stage, a small damage zone (green-yellow) appears in the gauge region near the fillet, where stress/strain energy is highest. This marks the onset of microcracking and stiffness locally begins to degrade but the rest of the specimen is still intact. In final fracture stage, the damage variable d reaches values close to 1 (red) in a narrow band across the gauge, indicating a fully developed crack that has effectively severed the cross-section. The surrounding blue region shows that failure is highly localised rather than diffuse. Fig. 10 depicts crack initiation and final fracture contours of all compositions. The phase-field simulations indicate that crack nucleation occurred consistently within the gauge section of the tensile specimen, corresponding to regions of maximum strain energy concentration.

For the PLA-HAp composite, damage initiation occurred at relatively low strain, reflecting limited strain energy storage or low toughness and predominantly brittle fracture response. MgO reinforcement progressively delayed onset, for instance 1 wt% showed stable, confined propagation, whereas 3 wt% further delayed initiation but exhibited abrupt localisation post-threshold, driving brittle failure despite peak strength (Fig. 9 bottom row). The rapid transition from elastic deformation to crack formation indicates that increased stiffness at this filler concentration promotes brittle-dominant fracture behaviour, despite delayed crack initiation. Higher loadings reversed this trend, for instance 5 wt%

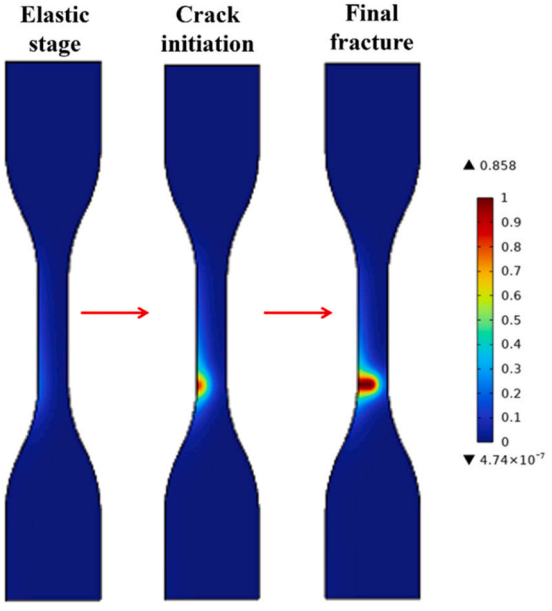


Fig. 9. Phase-field damage contours for crack evolution in PLA-HAp-MgO3 composite under uniaxial tensile loading: (a) elastic stage with no damage, (b) crack initiation at the gauge section, and (c) final fracture characterized by abrupt damage localisation and crack propagation.

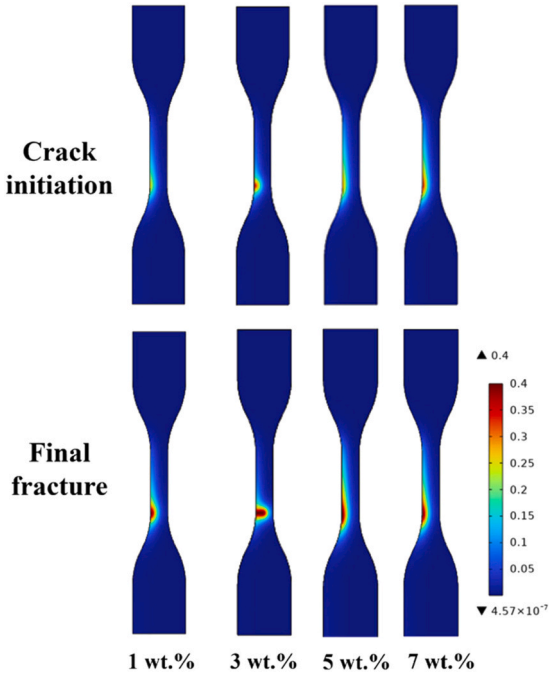


Fig. 10. Phase-field damage contours of crack initiation (top row) and final fracture (bottom row) in PLA-HAp-MgO composites under uniaxial tensile loading.

and 7 wt% MgO initiated cracks at elevated strains with gradual, diffuse propagation (smoother d-gradients), indicating enhanced energy storage and fracture stability despite lower strength. This matches SEM fracture morphology (Fig. 7), where ductile features is evidenced at low-mid MgO, and brittle cracks at extremes. The fracture patterns shown from the phase-field simulations were consistent with experimental findings of tensile behaviour and morphologies of fracture surface. Since direct experimental crack-path tracking and fracture-energy measurements were not performed, the phase-field simulations are interpreted qualitatively to compare relative crack initiation and propagation behaviour among compositions, rather than as a fully quantitative fracture validation.

It should be noted that the SEM observations and phase-field simulations describe different aspects of the fracture process. SEM images represent the final fracture surface and reveal local plastic deformation and energy dissipation, which are characteristic of ductile fracture features. In contrast, the phase-field model captures the evolution of crack initiation and propagation. For the PLA-HAp-MgO3 composite, improved stiffness and physical load sharing between the PLA matrix and dispersed inorganic fillers delayed crack initiation. However, once the critical strain-energy threshold was reached, damage rapidly localised within the gauge section, leading to abrupt crack propagation. Consequently, the composite exhibited ductile-like fracture features in SEM while still demonstrating brittle-dominant crack evolution in the phase-field simulations. In outset, the increase in MgO content delayed crack initiation and promoted more stable crack propagation, however, the PLA-HAp-MgO3 composite exhibited localized damage which indicates brittle-dominant fracture behaviour. These results suggests that MgO concentration in the composites play an important role in governing the balance between stiffness improvement and fracture stability.

3.8. Discussion

The experimental results demonstrate that the incorporation of dual HAp and MgO fillers significantly improves the mechanical, thermal, and fracture response of PLA composites. Among the investigated compositions, PLA-HAp-MgO3 shows increases of approximately 82% in

yield strength, 55% in ultimate tensile strength, and 54% in flexural strength compared with PLA-HAp. This improvement can be attributed to the combined effects of rigid-filler reinforcement, effective filler dispersion, physical filler-matrix contact, and restricted PLA chain mobility. Similar reinforcement effects have been reported for PLA/MgO-based systems, where MgO improved stiffness, strength, crystallization behaviour, and thermal response through filler-induced microstructural modification [13–16,20]. SEM morphology showed that low-to-moderate MgO contents produced relatively continuous surfaces with less obvious filler clustering, supporting improved load sharing between the PLA matrix and inorganic fillers. In contrast, excessive MgO loading, particularly at 7 wt%, promoted particle agglomeration, which created local stress-concentration sites and reduced the effective load-bearing capacity of the composite. This agrees with previous studies showing that nanoparticle agglomeration can reduce the reinforcing efficiency of PLA-based composites despite the high intrinsic stiffness of the filler phase [20,23,24].

The FTIR and XRD results provide important evidence for understanding the reinforcement mechanism. FTIR spectra showed the characteristic absorption bands of PLA and HAp without the formation of new bands or major peak shifts after MgO addition. Similar FTIR bands associated with PLA ester groups and phosphate groups from HAp have been reported in PLA- and HAp-containing composites [21,22,25]. Similarly, XRD patterns confirmed the retention of crystalline MgO/periclase-related reflections in MgO reinforced composites. But they did not show clear evidence of newly formed crystalline reaction products. These findings indicate that the enhancement in properties is not primarily caused by new chemical bonding or new crystalline reaction phases. Instead, the improvement is more reasonably explained by physical reinforcement, filler dispersion, physical filler–matrix contact, microstructural constraint, and the presence of thermally stable inorganic phases [13–16,20,23].

The thermal analysis further supports this interpretation. The DTG results show that the PLA-HAp-MgO composites generally exhibited a primary PLA degradation region at approximately 309-314 °C, with additional high-temperature degradation events around 466-488 °C in some compositions. PLA-HAp-MgO1 showed a main DTG peak at 313.0 °C, which agrees closely with its DSC peak at 314.3 °C, together with a weaker secondary event at 486.2 °C. PLA-HAp-MgO5 and PLA-HAp-MgO7 showed main DTG peaks at 309.2 °C and 313.6 °C, respectively, with secondary high-temperature events at 466.1 °C and 485.5 °C. The DSC peak of PLA-HAp-MgO7 at 319.2 °C also corresponds closely to its main DTG degradation region. The improved thermal response can be associated with the barrier effect of inorganic HAp and MgO phases, restricted polymer-chain mobility, and reduced mobility of degradation products within the filled polymer matrix. Similar thermal-stabilising effects have been reported in PLA-based composites containing inorganic fillers and MgO-based reinforcements [13–16,20,23].

Notably, PLA-HAp-MgO3 exhibited a distinct thermal degradation profile. Although a lower-temperature DTG event occurred at 310.8 °C, the strongest DTG peak appeared at 487.5 °C. This pronounced high-temperature DTG event, together with DSC events at 283.3 °C and 456.6 °C suggests improved resistance to rapid thermal degradation compared with the other MgO-reinforced compositions. This behaviour is consistent with the mechanical results, particularly 3 wt% MgO composition exhibited the highest tensile strength, yield strength, and flexural strength. Therefore, the combined thermal and mechanical findings indicate that 3 wt% MgO provides the most favourable balance between filler dispersion, physical filler–matrix contact, restricted PLA chain mobility, and thermal resistance. However, the PLA-HAp-MgO5 TGA curve showed an unrealistic negative residual mass at high temperature, indicating a baseline correction artefact. Therefore, its residual mass was not used for quantitative interpretation, although its DTG peak positions were still considered for identifying degradation events.

The numerical simulations further clarify the relationship between mechanical strengthening and fracture behaviour. The elastic finite element model reproduced the experimental tensile response with deviations below 5%, confirming that experimentally determined elastic properties can reliably predict the macroscopic stress response of the composites. The phase-field simulations provided additional insight into crack initiation and propagation, which cannot be fully captured from mechanical testing alone. The PLA-HAp-MgO3 composite delayed crack initiation due to improved stiffness and physical load sharing between the PLA matrix and dispersed inorganic fillers. However, once the critical strain-energy threshold was reached, damage rapidly localised within the gauge section, indicating brittle-dominant crack evolution despite the superior strength of this composition. In contrast, higher MgO loadings of 5-7 wt% promoted more diffuse crack propagation, suggesting improved fracture stability but lower strength due to agglomeration-induced weakening. This interpretation is consistent with the experimental SEM fracture morphology and with previous studies showing that filler dispersion strongly influences crack initiation, stress concentration, and fracture stability in PLA-based composites [20,23–25,31,32].

Overall, the results reveal a clear composition-dependent, stiffness-fracture stability trade-off. At 3 wt% MgO, filler dispersion and physical reinforcement are sufficient to maximise strength, stiffness, and thermal resistance, but the increased stiffness also promotes localised fracture once damage initiates. At higher MgO contents, agglomeration reduces strength and load-bearing efficiency, although crack propagation becomes more gradual. Therefore, the optimum composite design is not governed by MgO content alone, but by the balance between filler dispersion, rigid-particle reinforcement, thermal barrier effects, and crack-growth stability.

Fig. 11 presents the Ashby chart comparison of elastic modulus and tensile strength against density for the developed composites. Among all compositions, the composite with 3 wt% MgO exhibited the best balance of mechanical performance and lightweight characteristics, achieving a tensile strength of 51.36 MPa and elastic modulus of 4046.93 MPa. Compared with PLA-HAp, the addition of 3 wt% MgO increased tensile strength and elastic modulus by approximately 55% and 25%, respectively, while maintaining a low density within the polymer-composite region of the Ashby chart. The position of the 3 wt% MgO composites on the Ashby chart indicates an improved strength-to-weight ratio compared with the other compositions, moving it closer to the lower range of engineering polymer composites. This strength-to-weight balance suits biomedical implants, sustainable packaging, and lightweight automotive components, where thermal stability $T_{max} > 500°C$ adds value. However, additional biological and degradation studies are required before suitability for biomedical use can be confirmed.

4. Conclusion

This study investigated the mechanical, thermal, morphological, and fracture behaviour of PLA-HAp-MgO composites using experimental characterisation, finite element analysis, and phase-field fracture simulation. The results showed that 3 wt% MgO provided the optimum reinforcement level, increasing yield strength by approximately 82%, ultimate tensile strength by 55%, and flexural strength by 54% compared with PLA-HAp. The improvement was attributed mainly to rigid-filler reinforcement, effective filler dispersion, physical filler-matrix contact, restricted PLA chain mobility, and microstructural constraint rather than the formation of new chemical bonding. FTIR analysis showed no new absorption bands or major peak shifts after MgO incorporation, while XRD confirmed the retention of crystalline MgO-related phases without clear evidence of new crystalline reaction products. These findings support the conclusion that MgO acts primarily as a physically reinforcing and microstructurally modifying filler in the PLA-HAp matrix. Thermal analysis using TGA/DTG/DSC further showed that MgO addition modified the degradation behaviour of the composites. Most compositions exhibited a primary PLA degradation region at approximately 309-314 °C, while the PLA-HAp-MgO3 composite

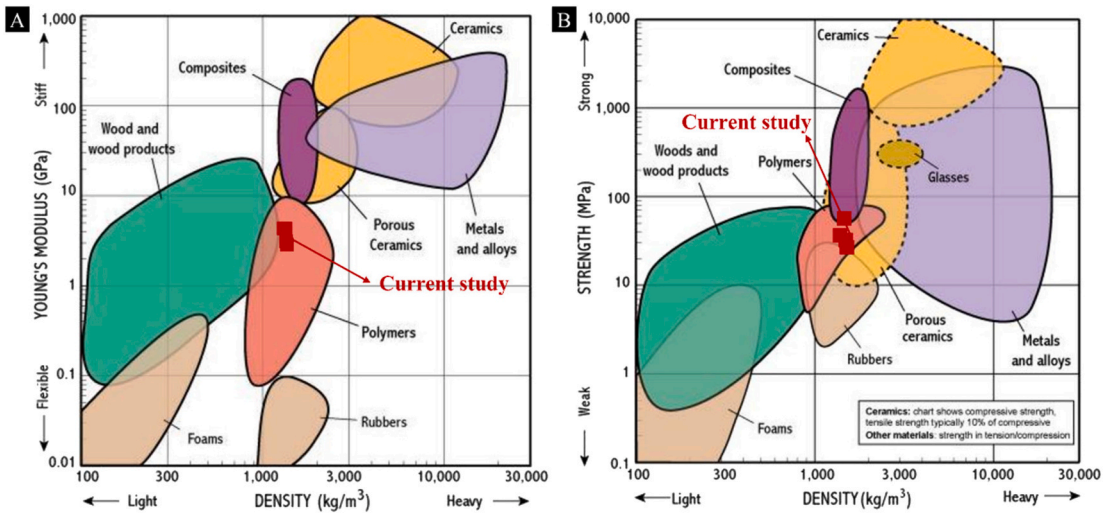


Fig. 11. Experimental data representation on Ashby chart (A) Elastic Modulus and (B) strength with respect to density.

showed a significant high-temperature DTG peak at 487.5 °C, supported by DSC curves at 283.3 °C and 456.6 °C. This indicates improved resistance to rapid mass loss and confirms that 3 wt% MgO provides the most favourable combined thermal and mechanical response. Finite element simulations reproduced the experimental tensile response with deviations below 5%, validating the reliability of the numerical model for predicting macroscopic stress behaviour. Phase-field fracture simulations revealed that PLA-HAp-MgO3 delayed crack initiation but exhibited abrupt damage localisation after the critical strain-energy threshold was reached. This indicates brittle-dominant crack evolution despite its superior strength. In contrast, higher MgO loadings of 5-7 wt % promoted more diffuse crack propagation and improved fracture stability but showed reduced mechanical strength due to particle agglomeration. Future work should evaluate biocompatibility, bioactivity, biodegradation behaviour, antibacterial effects, and fatigue resistance before considering clinical applications such as wound healing, orthopaedic implants, or dental devices.

Consent to participate

All authors voluntarily agree to participate in this research study.

Ethics declarations

The authors declare that they have no known competing financial interest or personal relationships that could have appeared to influence the work reported in this paper.

Consent for publication

All authors give the permission to the Journal to publish this research study.

Availability of data and materials

All data generated or analysed during this study are included in this published article.

Funding

This work was supported by CERVIE, UCSI University under a grant, T2S-2026/012.

Declaration of competing interest

The authors declare that they have no known competing financial interests or personal relationships that could have appeared to influence the work reported in this paper.

Acknowledgment

Not Applicable.

References

[1] Ramot Y, Haim-Zada M, Domb AJ, Nyska A. Biocompatibility and safety of PLA and its copolymers. Adv Drug Deliv Rev 2016;107:153–62. https://doi.org/10.1016/j.addr.2016.03.012.
[2] Casalini T, Rossi F, Castrovinci A, Perale G. A perspective on polylactic acid-based polymers use for nanoparticles synthesis and applications. Front Bioeng Biotechnol 2019;7:1–16. https://doi.org/10.3389/fbioe.2019.00259.
[3] Madhavan Nampoothiri K, Nair NR, John RP. An overview of the recent developments in polylactide (PLA) research. Bioresour Technol 2010;101:8493–501. https://doi.org/10.1016/j.biortech.2010.05.092.
[4] Nagarajan V, Mohanty AK, Misra M. Perspective on polylactic acid (PLA) based sustainable materials for durable applications: focus on toughness and heat resistance. ACS Sustainable Chem Eng 2016;4:2899–916. https://doi.org/10.1021/acssuschemeng.6b00321.
[5] Zhao X, Liu J, Li J, Liang X, Zhou W, Peng S. Strategies and techniques for improving heat resistance and mechanical performances of poly(lactic acid) (PLA) biodegradable materials. Int J Biol Macromol 2022;218:115–34. https://doi.org/10.1016/j.ijbiomac.2022.07.091.
[6] Hinchcliffe SA, Hess KM, Srubar WV. Experimental and theoretical investigation of prestressed natural fiber-reinforced polylactic acid (PLA) composite materials. Compos B Eng 2016;95:346–54. https://doi.org/10.1016/j.compositesb.2016.03.089.
[7] Aishah N, Bijarimi M, Moshiul AKM, Mat Desa MSZ, Norazmi M, Alhadadi W, Hafizah F, Nor MZM. Mechanical and thermal properties of binary blends poly lactic acid (PLA) and recycled high-density polyethylene (rHDPE). IOP Conf Ser Mater Sci Eng 2020;736. https://doi.org/10.1088/1757-899X/736/5/052022.
[8] Lu X, Tang L, Wang L, Zhao J, Li D, Wu Z, Xiao P. Morphology and properties of bio-based poly (lactic acid)/high-density polyethylene blends and their glass fiber reinforced composites. Polym Test 2016;54:90–7. https://doi.org/10.1016/j.polymertesting.2016.06.025.
[9] Suchanek W, Yoshimura M. Processing and properties of hydroxyapatite-based biomaterials for use as hard tissue replacement implants. J Mater Res 1998;13:94–117. https://doi.org/10.1557/JMR.1998.0015.
[10] Prakasam M, Locs J, Salma-Ancane K, Loca D, Largeteau A, Berzina-Cimdina L. Fabrication, properties and applications of dense hydroxyapatite: a review. J Funct Biomater 2015;6:1099–140. https://doi.org/10.3390/jfb6041099.
[11] Tsuchiya A, Sotome S, Asou Y, Kikuchi M, Koyama Y, Ogawa T, Tanaka J, Shinomiya K. Effects of pore size and implant volume of porous hydroxyapatite/collagen (HAp/Col) on bone formation in a rabbit bone defect model. J Med Dent Sci 2008;55:91–9.
[12] Murugan N, Murugan C, Sundramoorthy AK. In vitro and in vivo characterization of mineralized hydroxyapatite/polycaprolactone-graphene oxide based bioactive multifunctional coating on Ti alloy for bone implant applications. Arab J Chem 2018;11:959–69. https://doi.org/10.1016/j.arabjc.2018.03.020.

[13] Leonés A, Peponi L, Fiori S, Lieblich M. Effect of the addition of MgO nanoparticles on the thermally-activated shape memory behavior of plasticized PLA electrospun fibers. Polymers 2022;14. https://doi.org/10.3390/polym14132657.
[14] Liang H, Zhao Y, Yang J, Li X, Yang X, Sasikumar Y, Zhou Z, Chen M. Fabrication, crystalline behavior, mechanical property and in-vivo degradation of poly(l-lactide) (PLLA)-magnesium oxide whiskers (MgO) nano composites prepared by in-situ polymerization. Polymers 2019;11. https://doi.org/10.3390/polym11071123.
[15] Nikkhah Sokhanvar I, Karbalaei Ghomi NS, Mirmohammadi SA, Alihosseini A, Nasirian R. Enhancing poly(lactic acid)/maleated polypropylene blend with magnesium oxide catalyst: a reactive blending approach for improved mechanical properties. Int J Polym Anal Char 2024;29:253–68. https://doi.org/10.1080/1023666X.2024.2357555.
[16] Zhao Y, Liu B, You C, Chen M. Effects of MgO whiskers on mechanical properties and crystallization behavior of PLLA/MgO composites. Mater Des 2016;89:573–81. https://doi.org/10.1016/j.matdes.2015.09.157.
[17] Cament A, Moreno-Serna V, Loyo C, Quintana P, Seura P, Baier RV, Benavente R, Ulloa MT, Rivas LM, Pino E, Gómez T, Zapata PA. Mechanical and antimicrobial properties of low-density-polyethylene/MgO nanocomposites. Polym Adv Technol 2022;33:4355–70. https://doi.org/10.1002/pat.5865.
[18] Khanra AK, Jung HC, Yu SH, Hong KS, Shin KS. Microstructure and mechanical properties of Mg-HAP composites. Bull Mater Sci 2010;33:43–7. https://doi.org/10.1007/s12034-010-0006-z.
[19] Natarajan E, Ramesh S, Markandan K, Saravanakumar N, Dilip AA, Batcha ARS. Enhanced mechanical, tribological, and acoustical behavior of polyphenylene sulfide composites reinforced with zero-dimensional alumina. J Appl Polym Sci 2023;140. https://doi.org/10.1002/app.53748.
[20] Natarajan E, Sekar T, Markandan K, Nesappan S, Selvaraj ADA, Sekar SM. Structural integrity and mechanical behaviour of magnesium oxide (MgO) as reinforcement in PLA-HDPE composite. Emerg Mater 2024;7:1283–94. https://doi.org/10.1007/s42247-024-00650-z.
[21] Ercan F, Kayed TS, Kaygili O, Bulut N, Almohazey D, Ates T, Al-Ahmari FS, Ay I, Demirci T, Kirat G, Flemban T, İnce T, Ghrib T, Al-Suhaimi EA, Ercan I. Investigation of structural, spectroscopic, dielectric, magnetic, and in vitro biocompatibility properties of Sr/Ni co-doped hydroxyapatites. Ceram Int 2022;48:26585–607. https://doi.org/10.1016/j.ceramint.2022.05.354.
[22] Gamiz-Conde AK, Burelo M, Franco-Urquiza EA, Martínez-Franco E, Luna-Barcenas G, Bravo-Alfaro DA, Treviño-Quintanilla CD. Development and properties of bio-based polymer composites using PLA and untreated agro-industrial residues. Polym Test 2024;139. https://doi.org/10.1016/j.polymertesting.2024.108576.
[23] Swaroop C, Shukla M. Mechanical, optical and antibacterial properties of polylactic acid/polyethylene glycol films reinforced with MgO nanoparticles. Mater Today Proc 2018;5:20711–8. https://doi.org/10.1016/j.matpr.2018.06.455.
[24] Kotrotsos A, Yiallouros P, Kostopoulos V. Fabrication and characterization of polylactic acid electrospun scaffolds modified with multi-walled carbon nanotubes and hydroxyapatite nanoparticles. Biomimetics 2020;5:1–13. https://doi.org/10.3390/biomimetics5030043.
[25] Pandele AM, Constantinescu A, Radu IC, Miculescu F, Voicu SI, Ciocan LT. Synthesis and characterization of PLA-micro-structured hydroxyapatite composite films. Materials 2020;13:1–13. https://doi.org/10.3390/ma13020274.
[26] Chakravarty J, Rabbi F, Chalivendra V, Brigham CJ. Mechanical and biological properties of chitin/polylactide (PLA)/hydroxyapatite (HAP) composites cast using ionic liquid solutions. Int J Biol Macromol 2019. https://doi.org/10.1016/j.ijbiomac.2019.10.168.
[27] Sun S, Qin J, Zhuang Y, Cai P, Yu X, Wang H, Mo X, Wu J, EL-Newehy M, Abdulhameed MM, Fan M, Qian W, Sun B. Development of MgO-loaded PLA/dECM antibacterial nanofibrous membranes for enhanced gingival regeneration. Biomater Sci 2025;13:3354–66. https://doi.org/10.1039/d4bm01346h.
[28] Komeijani M, Bahri-Laleh N, Mirjafary Z, D'Alterio MC, Rouhani M, Sakhaeinia H, Moghaddam AH, Mirmohammadi SA, Poater A. PLA/PMMA reactive blending in the presence of MgO as an exchange reaction catalyst. Polymers 2025;17. https://doi.org/10.3390/polym17070845.
[29] Hirshikesh, S. N., Natarajan, S., Annabattula, R. K., & Martínez-Pañeda, E. Phase field modelling of crack propagation in functionally graded materials. Compos B Eng, 169, 239–248. https://doi.org/10.1016/j.compositesb.2019.04.003.
[30] Egger, A., Pillai, U., Agathos, K., Kakouris, E., Chatzi, E., Aschroft, I. A., & Triantafyllou, S. P. Discrete and phase field methods for linear elastic fracture mechanics: a comparative study and state-of-the-art review. Appl Sci, 9(12), 2436. https://doi.org/10.3390/app9122436.
[31] Rajeshkumar G, Arvindh Seshadri S, Devnani GL, Sanjay MR, Siengchin S, Prakash Maran J, Al-Dhabi NA, Karuppiah P, Mariadhas VA, Sivarajasekar N, Ronaldo Anuf A. Environment friendly, renewable and sustainable poly lactic acid (PLA) based natural fiber reinforced composites – a comprehensive review. J Clean Prod 2021;310:127483. https://doi.org/10.1016/j.jclepro.2021.127483.
[32] Mondal S, Nguyen TP, Pham VH, Hoang G, Manivasagan P, Kim MH, Nam SY, Oh J. Hydroxyapatite nano bioceramics optimized 3D printed poly lactic acid scaffold for bone tissue engineering application. Ceram Int 2020;46:3443–55. https://doi.org/10.1016/j.ceramint.2019.10.057.